Strain-tunable magnetic compensation temperature of epitaxial $Tb_3Fe_5O_{12}$ thin films

Yufei Li,[1,*] Xihui Yang,[2,*] Hua Bai,[3] Mingzhi Wang,[1] Dashuai Cheng,[1] Cheng Song,[3] Zhe Yuan,[4] Yi Liu,[2,†] and Zhong Shi[1,‡]

[1]*Shanghai Key Laboratory of Special Artificial Microstructure Materials and Technology and Pohl Institute of Solid State Physics and School of Physics Science and Engineering, Tongji University, Shanghai 200092, China*

[2]*Center for Advanced Quantum Studies and Department of Physics, Beijing Normal University, Beijing 100875, China*

[3]*Key Laboratory of Advanced Materials, School of Materials Science and Engineering, Beijing Innovation Center for Future Chips, Tsinghua University, Beijing 100084, China*

[4]*Institute for Nanoelectronic Devices and Quantum Computing, Fudan University, Shanghai 200433, China*

(Received 7 May 2023; revised 7 September 2023; accepted 16 October 2023; published 7 November 2023)

High-quality rare-earth iron garnet (ReIG) $Tb_3Fe_5O_{12}$ (TbIG) thin films are epitaxially grown on a series of (111)-oriented garnet substrates with various lattice constants. The coherent growth induces a substrate-dependent in-plane tensile or compressive strain in the TbIG film. Measurements of the anomalous Hall-like effect in TbIG/Pt heterostructures show that the compensation temperature of TbIG films monotonically changes with the film strain. The strain results in a variation of the distances between magnetic atoms in the TbIG crystal and therefore the corresponding exchange interactions. The latter is explicitly calculated as a function of the lattice strain based on density-functional theory, reproducing the observed experimental results. This work provides a versatile way to optimize ReIG-based spin-orbit torque devices.

DOI: 10.1103/PhysRevB.108.184403

I. INTRODUCTION

Ferrimagnetic rare-earth iron garnets (ReIGs) containing coupled sublattices with inequivalent and antiparallel magnetic moments have attracted intensive research interest for their potential applications in the next generation of spintronic devices [1–4]. As typical ferrimagnets, the most common feature of ReIGs is the magnetic compensation point, where the magnetic moment of the rare earth (M_{Re}) is equal to that of iron (M_{Fe}) resulting in a vanishing remanent net magnetization. This characteristic of the ferrimagnets at the compensation point imparts upon them certain properties of antiferromagnetic materials, such as large coercive field [5], enhanced exchange coupling [6], and long spin coherence length [7,8]. Therefore, near the magnetic compensation point, ReIGs enable fast spin-orbit torque (SOT) switching [9], ultralow switching current [10], and offer promising properties such as low energy consumption, high efficiency, and robustness, making them compelling candidates for advanced spintronic applications. Meanwhile, the magnetization of sublattices can be individually distinguished using the magneto-optical effect [11–13] or electric transport effects such as spin Hall magnetoresistance [14,15]. This approach is promising for facilitating investigation of the exchange interactions within and among the sublattices, which primarily determine the compensation point, and provides insights into the underlying physics of ferrimagnetic materials [16–18].

To tune the compensation point, conventional ferrimagnetic alloys have been adjusted by altering the composition ratio [19,20]. In the context of ReIGs, the approaches to manipulate the compensation temperature entails replacing trivalent rare-earth ions (such as Gd^{3+}, Tb^{3+}, Dy^{3+}, and Tm^{3+}) at the relevant dodecahedron site, and/or replacing the iron ions at the tetrahedron/octahedron sites [21–23]. Very recently, a strain-tunable effect on the Néel temperature was observed in perovskite $YCrO_3$ thin films by inducing lattice strain from the substrate [24]. This demonstrates that strain has the ability to significantly alter the lattice constant, offering a powerful tool to control the compensation point without varying the chemical composition. Here, we implement this idea by performing a systematic study of the strain effect on the compensation temperature in ReIGs.

Terbium iron garnet ($Tb_3Fe_5O_{12}$, TbIG) has a larger positive magnetostriction constant ($\lambda_{111} = 1.2 \times 10^{-5}$) than the other ReIGs at room temperature [25,26]. Thus, a strain effect on the compensation temperature is expected to be tuned over a wide range in TbIG. In this paper, high-quality epitaxial TbIG thin films are grown on (111)-oriented single-crystalline garnet substrates, which introduce a systematic variation in the lattice strain of the TbIG films. By measuring the anomalous Hall-like effect (AHLE) in TbIG/Pt heterostructures as a function of temperature, we find that the compensation temperature (T_{comp}) of TbIG monotonically decreases with increasing lattice constant of the substrate. Using density-functional theory, we explicitly calculate the exchange interactions between magnetic atoms in TbIG as a function of the lattice strain, which reproduces the observed variation in T_{comp} in our experiment. For other rare-earth iron garnets, where the rare-earth ions have finite magnetic moments, the strain-tunable effect on the compensation temperature is also expected. The current results provide deeper

*These authors contributed equally to this work.
†yiliu@bnu.edu.cn
‡shizhong@tongji.edu.cn

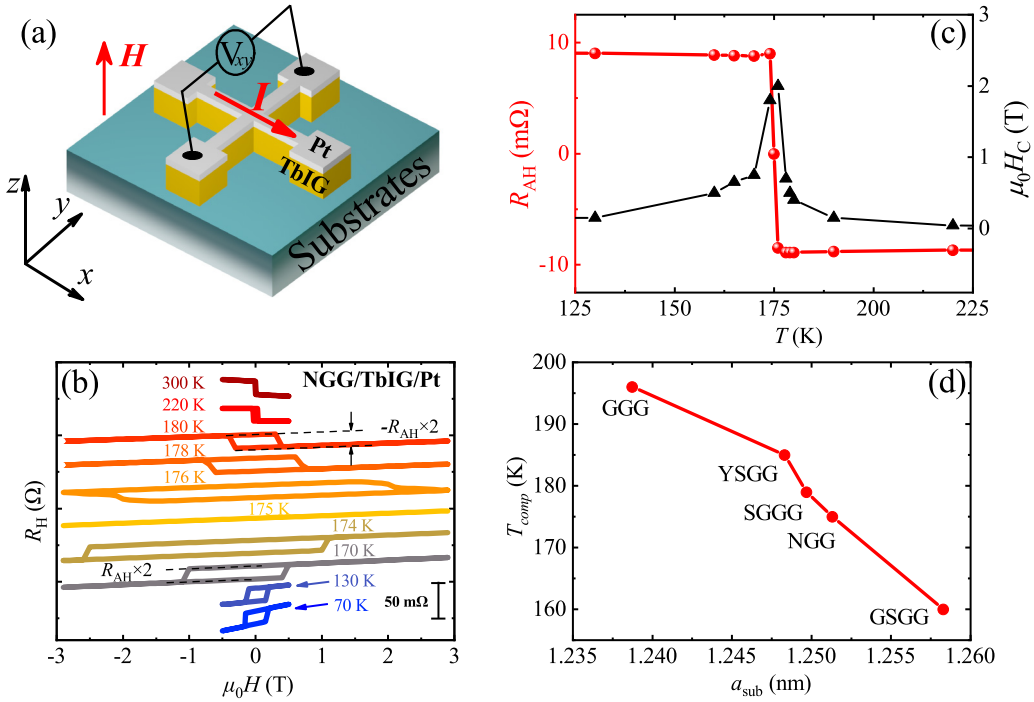

FIG. 1. (a) Schematic geometry of transport measurement on TbIG/Pt heterostructure. (b) Hall resistance (R_H) vs applied magnetic field for TbIG/Pt on NGG substrate at various temperatures. R_{AH} is defined as half of R_H jump at y axis, as indicated by black dashed lines at 170 and 180 K. (c) R_{AH} (circles) and coercivity ($\mu_0 H_C$) (triangles) as function of temperature for NGG/TbIG/Pt extracted from transport measurement. (d) T_{comp} for TbIG on different substrates as function of lattice constant of garnet substrate.

insight for controlling the magnetic properties in ferrimagnetic materials and are helpful for facilitating the application of ReIG-based SOT devices.

II. SAMPLE PREPARATION

Five kinds of (111)-oriented single-crystalline garnet substrates, including $Gd_3Ga_5O_{12}$ (GGG), $Y_3Sc_2Ga_3O_{12}$ (YSGG), $Gd_{2.6}Ca_{0.4}Ga_{4.1}Mg_{0.25}Zr_{0.65}O_{12}$ (SGGG), $Nd_3Ga_5O_{12}$ (NGG), and $Gd_3Sc_2Ga_3O_{12}$ (GSGG), were selected for deposition of 20-nm-thick TbIG films by pulsed laser deposition (PLD). Every batch of five substrates was precleaned, subsequently affixed to a circular sample stage at the same time, and evenly distributed in a circle. The sample stage was then transferred into the PLD chamber of a PLD-sputtering linked system. The base pressure of the PLD chamber was less than 2×10^{-6} Pa, and the substrates were preheated to and kept at 750 °C for 1 h before film deposition. During deposition, a KrF ($\lambda = 248$ nm) excimer pulsed laser with a laser fluence $\sim 1.22\,\mathrm{J/cm^2}$ was used to strike a stoichiometric polycrystalline TbIG target with a repetition rate of 4 Hz in a PLD chamber atmosphere of 3.0-Pa oxygen. To ensure the homogeneous growth of samples in one batch, the sample stage rotates clockwise at a certain rate ω_1 during deposition, with the laser plasma plume swept over the center of each substrate (see more details in Fig. S1(a) of Supplemental Material [27]). Twenty-nanometer-thick TbIG films were simultaneously deposited on the five substrates with a growth rate of 0.33 Å/s. The batch of films was then crystalized by *in situ* annealing at 750 °C for another 2 h in a pure oxygen atmosphere of 6×10^4 Pa. After that, the samples were cooled to room temperature and transferred to the magnetron sputtering chamber without breaking vacuum. A 3-nm-thick platinum (Pt) layer was deposited on each TbIG film at room temperature by magnetron sputtering with a 0.4-Pa Ar pressure. The deposition rate of Pt was 0.68 Å/s. UV lithography and ion-beam etching were employed on these substrate/TbIG (20 nm)/Pt (3 nm) samples to fabricate identical Hall-bar patterns for the subsequent electric transport measurements. Another batch of 20-nm-thick TbIG films without Pt capping layers was also grown for crystallographic characterization and magnetometry measurements.

III. ELECTRIC TRANSPORT AND MAGNETOSTATIC MEASUREMENTS

We first carried out transport measurements of the TbIG (20 nm)/Pt (3 nm) heterostructures on the five different substrates. Figure 1(a) depicts a schematic of the device geometry. The driven current I flowed into the Pt layer in the x direction, and the magnetic field H was applied in the z direction. Then, the Hall voltage was detected in the y direction by a VersaLab system in the temperature range from 70 to 300 K. In TbIG/Pt heterostructure, the magnetic proximity effect in Pt layer, induced by the nearby magnetic TbIG layer via exchange interaction, can generate an anomalous Hall voltage. In addition, the inverse spin Hall effect also leads to an AHLE signal depending on the spin-mixing conductance of the TbIG/Pt interface [28,29]. All the AHLE signals are essentially determined by the magnetization of Fe^{3+} in TbIG

since the $3d$ electrons are much more extended than the $4f$ electrons in Tb^{3+}. Therefore, the observed anomalous Hall-like signal primarily reflects the magnetic properties of Fe^{3+}.

Taking NGG/TbIG/Pt as an example, the magnetic field dependence of the Hall resistance (R_H) at various temperatures is plotted in Fig. 1(b). The R_H - H loops of NGG/TbIG/Pt exhibit square shapes with sharp jumps at all temperatures except for 175 K due to the well-established PMA in TbIG grown on the NGG substrate. This is similar to previous works on ReIG/Pt heterostructures with PMA [11,28,30–34]. Therefore, we can extract the anomalous Hall-like spin Hall resistance (R_{AH}) by calculating $R_{\mathrm{AH}} = (R_H{}^+ - R_H{}^-)/2$, where $R_H{}^+$ and $R_H{}^-$ are the two intersection points with the y axis obtained by extrapolating the R_H - H loop at positive and negative saturated fields, as marked by the dashed lines in Fig. 1(b). As the temperature increases, R_{AH} abruptly changes sign from positive to negative at 175 K. This is because as the temperature increases across T_{comp}, the magnetization of Fe^{3+} becomes larger than that of Tb^{3+} such that the magnetic moments on Fe^{3+} reverse to guarantee the net magnetization to be aligned with the external magnetic field. Thus, the measured Hall voltage reverses at T_{comp} of TbIG [35]. In particular, when the magnetization in the ferrimagnet is just compensated at T_{comp}, the system has zero net magnetization resulting in the divergent coercive field.

It is worth noting that the sign change of R_{AH} occurs in a very narrow temperature window. As shown in Fig. 1(b), R_{AH} approaches zero at 175 K, exhibiting a straight line in the R_H - H curve. However, a negative (positive) R_{AH} with a square loop resurges at 176 K (174 K), only 1 K away from T_{comp}. Therefore, the sign change of R_{AH} for the NGG/TbIG/Pt heterostructure can be used to determine the T_{comp} of TbIG with a precision of 1 K, as shown by the red circles in Fig. 1(c). The coercive field of the TbIG film on NGG is plotted as the black triangles in Fig. 1(c), which tends to diverge at 175 K, in agreement with the R_{AH} measurement.

To verify the T_{comp} determined by the AHLE, we further measured the temperature-dependent magnetization and coercivity of the TbIG film on NGG by a vibrating sample magnetometer (see Fig. S2 in Supplemental Material [27]). However, due to the near-zero net magnetization of the TbIG film itself in the vicinity of T_{comp} and the substantial paramagnetic signal originating from the NGG substrate, it is a challenge to extract the net magnetization data from TbIG film within the temperature close to T_{comp}. Therefore, the sign-change temperature of R_{AH} is a better estimate for the T_{comp} of TbIG due to its sensitivity and accuracy. On different garnet substrates (see more details in Fig. S3 of Supplemental Material [27]), T_{comp} is 160 K (GSGG), 175 K (NGG), 179 K (SGGG), 185 K (YSGG), and 196 K (GGG), as shown in Fig. 1(d), where the T_{comp} of TbIG is found to monotonically decrease with increasing lattice constant of the substrate.

IV. STRUCTURE AND STRAIN CHARACTERIZATION

T_{comp} is primarily dominated by the exchange interactions within and among the magnetic Tb and Fe ions in TbIG, which are varied by the lattice distortion due to the different substrates. To determine the relationship between the T_{comp} of TbIG and the lattice constant of the relevant substrates, we investigated the morphology of bare TbIG films without Pt capping layers. The film thickness was characterized at room temperature by x-ray reflection, which confirmed the consistent thickness of 20 nm for all the films on the five different substrates, and the root-mean-square surface roughness was less than 2 Å as measured by atomic force microscopy. To examine the epitaxial growth and crystalline ordering, we performed cross-sectional high-angle annular dark-field (HAADF) imaging of the TbIG film on GGG (111) viewed along the $[1\bar{1}0]$ direction using scanning transmission electron microscopy (STEM), as shown in Fig. 2(a). The STEM image shows high-quality epitaxy of the TbIG film throughout the whole region. The yellow dashed line indicates the GGG/TbIG atomically sharp interface with perfect continuation of the garnet lattice, without any detectable dislocations or other defects. The sharp interface and homogeneity are further confirmed from the element distribution analysis by energy-dispersive x-ray spectroscopy (see more details in Figs. S1(b) to S1(d) and Table S1 of Supplemental Material [27]).

A conventional parameter η is usually adopted to characterize the lattice strain and deformation induced by the lattice mismatch between the TbIG film and substrate as $\eta = \frac{a_{\mathrm{sub}} - a_{\mathrm{TbIG}}}{a_{\mathrm{TbIG}}}$, where a_{sub} and a_{TbIG} are the lattice constants of the substrate and TbIG bulk material, respectively [26,36–38] (here, $a_{\mathrm{TbIG}} = 1.2460$ nm from Ref. [26]). To describe the distortion of TbIG, we must also consider the out-of-plane strain in the TbIG film in addition to the in-plane strain parameter η. As shown in Fig. 2(b), the x-ray diffraction (XRD) curves taken from the TbIG films on various substrates show two main (444) Bragg peaks for the TbIG films (marked by up arrows) and garnet substrates. Laue oscillations around film peaks indicate the precise spatial periodicity of the epitaxial TbIG lattice, and smooth interfaces on the corresponding substrates. The Bragg peaks of the substrates shift towards the right-hand side from GSGG to GGG, corresponding to the monotonically decreasing lattice spacing d_{444}^{sub}. The lattice constants a_{sub} are derived and listed in Table I. In contrast, the (444) Bragg peaks of the TbIG films (up arrows) shift towards the left-hand side to a lower angle with decreasing substrate lattice spacing from GSGG to GGG. In particular, the peak of TbIG on GSGG shows a distinct crossover as it moves to the right-hand side of the GSGG peak. The diffraction peaks suggest that for the TbIG films, there are opposite variations in the in-plane lattice spacing controlled by the substrate and the out-of-plane lattice spacing, as listed by d_{444}^{TbIG} in Table I. The epitaxial growth of TbIG exhibits anisotropic distortion compared with the bulk structure. Similar phenomena have also been observed in previous reports [38,39]. Thus, the parameter η is not sufficient to characterize the lattice distortion or distinguish the in-plane and out-of-plane strain of TbIG.

To elucidate the lattice distortion and strain distribution, reciprocal-space mapping (RSM) was performed around the (624) asymmetric peaks of TbIG on GGG and GSGG, corresponding to the lower and upper bounds of the in-plane lattice constant in the series of garnet substrates, and the results are shown in Figs. 2(c) and 2(d), respectively. This RSM plot provides rich structural information of the TbIG films on the substrates. First, the lattice spacings d_{220} and d_{444} calculated from the RSM plot of GGG (GSGG) are in

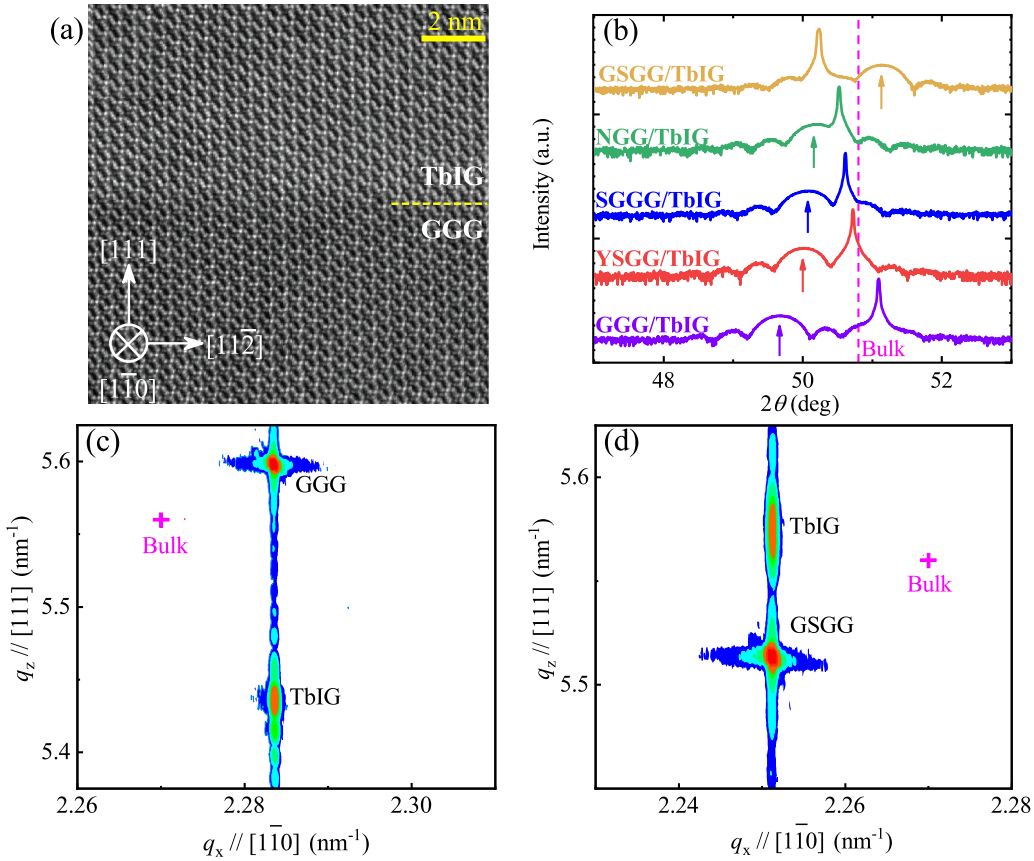

FIG. 2. (a) Cross-sectional HAADF-STEM image of TbIG film grown on (111)-oriented GGG, viewed along [1$\bar{1}$0] direction. (b) X-ray-diffraction patterns of 20-nm-thick TbIG films deposited on (111)-oriented GGG, YSGG, SGGG, NGG, and GSGG. Curves are vertically offset for clarification. Up arrows represent position of (444) Bragg peaks of TbIG films. Dashed line indicates (444) Bragg peak of bulk TbIG [26]. Reciprocal-space mappings of asymmetric scan around (624) peaks of TbIG films on GGG (c) and GSGG (d) substrates. Crosses show calculated peak positions for bulk cubic TbIG.

good agreement with the lattice constant of $a_{GGG} = 1.238$ nm ($a_{GSGG} = 1.257$ nm) for the cubic GGG (GSGG) crystal. Second, the RSMs reveal that the q_x//[1$\bar{1}$0] orientation of the TbIG film is nearly identical to those of the GGG and GSGG substrates, suggesting that the TbIG films grow coherently within the plane and adopt the lattice constant of the substrate. Since GGG and GSGG are the lower and upper limits for the lattice constant of the five substrates, it is reasonable to believe that all the TbIG films are in-plane fully strained to YSGG, SGGG, and NGG [38,39]. Moreover, the RSM plot of the TbIG layer on GGG (GSGG) is below (above) that of the substrate along the q_z//[111] direction, indicating that the out-of-plane lattice spacing is larger (smaller) than that of the substrate. Therefore, the TbIG film is deformed with a compressive (tensile) strain on the GGG (GSGG) substrate, leading to an increase (decrease) in the out-of-plane lattice spacing (d_{444}) for the film.

TABLE I. Structural parameters and compensation temperatures for TbIG thin films grown on different substrates. Lattice constant of substrates (a_{sub}) and out-of-plane lattice spacing of TbIG (d_{444}^{TbIG}) are determined by XRD. Parameter η is derived from a_{sub} and bulk TbIG lattice constant ($a = 1.2460$ nm) [26]. T_{comp} is determined from R_{AH} - T curves.

Substrate	a_{sub} (nm)	η (%)	d_{444}^{TbIG} (nm)	T_{comp} (K)
GGG	1.23757	−0.67658	0.18338	196
YSGG	1.24599	0.00872	0.1822	185
SGGG	1.24852	0.20249	0.18201	179
NGG	1.25049	0.35997	0.18165	175
GSGG	1.25711	0.89202	0.17843	160

To explicate the variation of out-of-plane lattice distance, we prepared TbIG films with different thickness on GSGG substrate, of which the (444) diffraction peaks are shown in Fig. S4 of Supplemental Material [27]. With the film thickness increasing, the out-of-plane lattice spacing d_{444} is gradually approaching the bulk value. In our transport measurement, the AHLE signals are essentially determined by the magnetization of Fe^{3+} in the TbIG layer adjacent to the Pt, which would have the least out-of-plane distortion. Therefore, without loss of generality, the structure of the topmost TbIG layer is theoretically modeled in the following as a fully strained in-plane lattice that matches the corresponding substrate, while the out-of-plane lattice spacing is assumed to be that of bulk TbIG.

V. THEORETICAL CALCULATIONS

Typically the compensation temperature of a ferrimagnet is determined by the competition between the magnetization of sublattices in mean-field theory [21,40,41], where the most important parameters are the exchange interactions within and among each sublattice. To investigate the effects of the lattice structure on $T_{\rm comp}$, we first calculate the exchange interactions in ferrimagnetic TbIG based on density-functional theory. In a crystal cell of TbIG, there are three types of magnetic ions associated with different coordination polyhedra of oxygen ions: 24 Tb ions in dodecahedra (the c sites), 16 Fe^{O} ions in octahedra (the a sites), and 24 Fe^{T} ions in tetrahedra (the d sites). Thus, there are five exchange parameters among the sublattices [42,43]: the J_{ad} between the two nearest Fe ions that belong to the two types of Fe with antiparallel atomic magnetizations, the J_{aa} and J_{dd} between the nearest Fe^{O} at the a sites and the nearest Fe^{T} at the d sites, respectively, and the J_{ac} and J_{dc} between the rare-earth atom and the two types of Fe ions, respectively. We can map the total energy as

$$E_{\rm tot} = E_0 + \frac{1}{2}\sum_{i\neq j} J_{ij}\boldsymbol{\mu}_i \cdot \boldsymbol{\mu}_j, \tag{1}$$

where E_0 is the magnetization-independent energy of the system and $\boldsymbol{\mu}_i$ is the atomic magnetization of the ith magnetic ion. The exchange interactions J_{ij} are considered short ranged, and only the five types discussed above are taken into account. We artificially construct eight inequivalent collinear spin configurations with atomic magnetizations flipped at different sites (see more details in Fig. S5 in Supplemental Material [27]). The total energies of these configurations are calculated from first principles (see more details in Table S2 in Supplemental Material [27]), and a least-squares fit [42–45] using Eq. (1) determines the values of the exchange interactions.

The total energy calculation is carried out using the Vienna *Ab initio* Simulation Package (VASP) [46,47]. The Perdew-Burke-Ernzerhof (PBE) [48] functional is employed to describe the exchange and correlation effect. A PBE version of the all-electronic projector augmented-wave method [49] is adopted with the $3d^6\ 4s^2$ configuration of Fe, $4f^9\ 6s^2$ configuration of Tb and $2s^2\ 2p^4$ configuration of O treated as valence electrons. An on-site Coulomb correction is employed with the Hubbard U and Hund's J parameters chosen as $U-J = 4.7$ eV for Fe ions and $U-J = 3.3$ eV for Tb ions [50]. A gamma-centered k-point mesh of $11\times11\times11$ is used to sample the Brillouin zone, and the cutoff energy of the plane-wave basis vector is chosen as 700 eV. The above parameters have been tested for convergence. The choice of the Hubbard U and Hund's J parameters does not influence our magnetic ground state, and the calculated magnetization is found to be insensitive to the specific $U-J$ values.

The calculated exchange interactions as a function of the bond length are plotted using solid symbols in Fig. 3. Shaded areas mark corresponding value ranges according to computational uncertainties. It is assumed that TbIG maintains the body-centered cubic (bcc) crystal structure, but its lattice constant is chosen to match that of the substrate. Our calculated exchange coefficients (black cross) agree reasonably well with the experimentally fitted values of bulk TbIG [51], where the most important $J_{ad} = 2.62$ meV was extracted from

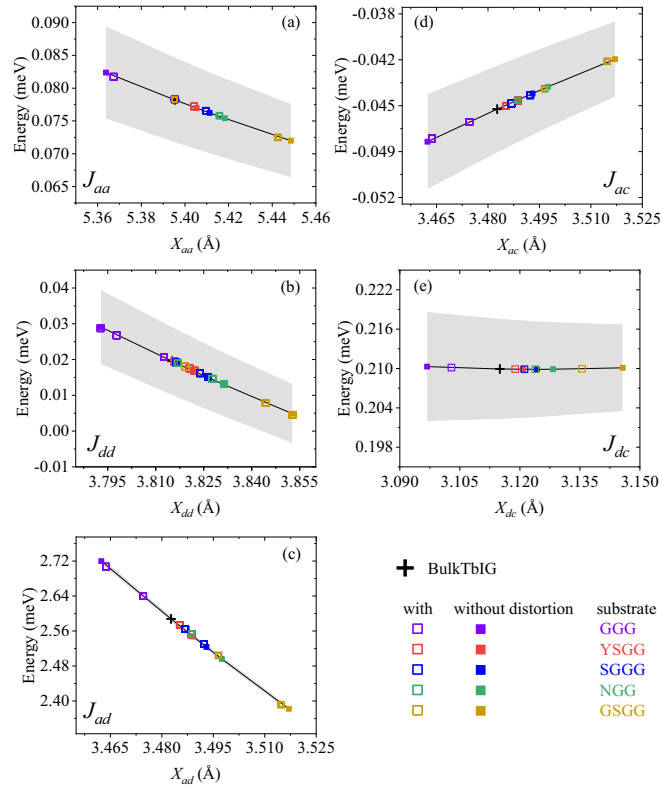

FIG. 3. Calculated exchange interactions between nearest atomic magnetizations in TbIG as a function of the corresponding bond length. Solid symbols present values for bcc TbIG with lattice constant same as substrates. Open symbols mark values interpolated from solid symbols corresponding to changed bond lengths when lattice distortion is taken into account. Shaded areas mark standard deviations of calculated values.

experimental measurement compared to our calculated value of 2.59 meV. When the lattice constant of the substrates, as listed in Table I, is imposed on the TbIG lattice, TbIG becomes compressed (on the GGG substrate) and expanded (on the other four substrates) accordingly. Then, the calculated exchange-interaction coefficients, as shown by the solid symbols in Fig. 3, monotonically decrease with the bond length or lattice constant. It is worth mentioning that all the relevant bond angles are not changed with the bcc structure maintained.

It is straightforward to divide these exchange coupling into two categories: Fe^{3+}-Fe^{3+} (or $3d^5-3d^5$) coupling, namely J_{aa}, J_{dd}, and J_{ad} as shown in Figs. 3(a)–3(c) (left column), and $Fe^{3+}-Tb^{3+}$ (or $3d^5-4f^8$) coupling, namely J_{ac} and J_{dc} as shown in Figs. 3(d) and 3(e) (right). The former ones are antiferromagnetic (AFM) superexchange coupling according to the Goodenough-Kanamori-Anderson rule [52–54], expressed in terms of positive exchange coefficients in our formalism. Their magnitude is determined by the corresponding bond lengths. Increasing the lattice constant leads to decrease in all three of them. For the latter category, our calculated results show that the exchange type is more intuitive: with the atomic magnetizations parallel with each other, the exchange, J_{ac}, between Fe^{O} and Tb ions is ferromagnetic (FM), while the exchange, J_{dc}, between Fe^{T} and Tb ions is AFM with

their magnetizations antiparallel. The FM J_{ac} also decreases linearly with increasing bond length, but the AFM J_{dc} keeps almost constant. This insensitivity to bond length may result from its significantly short bond length (the shortest one among the five); the overlap integral of electronic orbitals that determines the exchange strength is nearly unchanged as the lattice size varies in the region we studied.

Our calculated exchange coefficients are reasonably consistent with the reported values in literature. The dominant positive value of J_{ad} results in the antiferromagnetic coupling of Fe^O and Fe^T ions, as in many iron garnets [42,50,51,55–57]. In addition, our calculated J_{dc} is positive in agreement with the positive values in these experimental and theoretical studies for GdIG [42,50,51,55–57], NdIG [50], and TbIG [51]. For the exchange coefficient J_{ac}, we find a small negative value indicating the weak ferromagnetic coupling between Fe^O and Tb ions. The negative sign is the same as the calculated J_{ac} in GdIG, but is opposite to the extracted value for TbIG [51]. The difference can be attributed to the approximation applied in fitting the experimental susceptibility that J_{ad}, J_{aa}, and J_{dd} were assumed to be the same as in yttrium iron garnet (YIG). In fact, both the studies of YIG [45] and GdIG [42] demonstrate that the exchange coefficients sensitively depend on the lattice constant. Therefore, quantitative values of the exchange coefficients in ReIG must be carefully treated by taking the corresponding lattice structure and electronic properties into account.

We further take into account the anisotropic lattice distortion: the in-plane lattice constant is the same as that of the substrate, but the out-of-plane layer distance along the film-normal direction remains the same as that in the bulk TbIG. For the five different substrates, we determine their changed bond lengths for every pair of magnetic ions. Interpolating along the lines in Fig. 3 using these bond lengths, we obtain modified exchange interactions (open symbols) due to anisotropic lattice distortion. For each type of exchange, there can be in principle as many different values as the number of pairs. In the simplest case, as for J_{aa}, every Fe^O ion has eight nearest neighbors of the same sublattice in the original bcc structure. Lattice distortion divides these neighboring pairs into two categories, as shown in Fig. 3(a): one category has similar bond length to that in the substrate due to the in-plane lattice matching, while the other has the same bond length as that in bulk TbIG resulting from the out-of-plane layer distance. Therefore, as shown in Fig. 3(a), there are five open symbols along the J_{aa} value line, and the other five superposed on the cross stand for bulk TbIG. The situation is significantly different for other exchange-interaction parameters, as there can be more bond lengths for other pairs of magnetic ions.

With the exchange interaction of every ion pair determined, we obtain the average exchange parameters for each sublattice and calculate the compensation temperature, T_{comp}, within mean-field theory [21,41]. Each atomic magnetization of sublattices Fe^O, Fe^T, and Tb is subject to the mean exchange field from the magnetizations of its neighbors:

$$H_a = -\left[\tilde{J}_{aa}\cdot M_a(T) + \tfrac{1}{2}\tilde{J}_{ad}\cdot M_d(T) + \tfrac{1}{2}\tilde{J}_{ac}\cdot M_c(T)\right], \quad (2)$$

$$H_d = -\left[\tfrac{1}{3}\tilde{J}_{dd}\cdot M_d(T) + \tfrac{1}{2}\tilde{J}_{ad}\cdot M_a(T) + \tfrac{1}{6}\tilde{J}_{dc}\cdot M_c(T)\right], \quad (3)$$

$$H_c = -\left[\tfrac{1}{2}\tilde{J}_{ac}\cdot M_a(T) + \tfrac{1}{6}\tilde{J}_{dc}\cdot M_d(T)\right]. \quad (4)$$

Here, all the parameters $\tilde{J}$ represent the average values of the different exchange interactions, and H_ξ and $M_\xi(T)$ are the effective field and the total magnetization of the Fe^O ($\xi = a$), Fe^T ($\xi = d$), and Tb ($\xi = c$) sublattices, respectively. The magnetization as a function of temperature is expressed in terms of the Brillouin function $B_S(x)$:

$$M_\xi(T) = N_\xi|\mu_\xi|B_S(x_\xi), \quad (5)$$

$$B_S(x_\xi) = \frac{2S_\xi+1}{2S_\xi}\coth\left(\frac{2S_\xi+1}{2S_\xi}x_\xi\right) - \frac{1}{2S_\xi}\coth\left(\frac{1}{2S_\xi}x_\xi\right) \quad (6)$$

$$x_\xi = |\mu_\xi|H_\xi/(k_BT), \quad (7)$$

where N_ξ is the number of ions within each sublattice in the unit cell ($N_a = 8$, $N_d = N_c = 12$), μ_ξ is the atomic magnetization ($\mu_a = 5$, $\mu_d = -5$, $\mu_c = 6$, in the unit of the Bohr magneton μ_B), $S_a = S_d = 5/2$ is the spin of Fe ions, and $S_c = 3$ for Tb ions. It is worth mentioning that the single-ion anisotropy field on Tb ions of approximately 1 T (estimated from the saturation field along the hard axis in Fig. S6) is neglected in our mean-field theory since it is much smaller than the exchange fields.

Solving Eqs. (2)–(7) self-consistently, we can calculate the magnetization $M_\xi(T)$ at every temperature. The total magnetization of the system,

$$M_{tot}(T) = M_a(T) + M_d(T) + M_c(T), \quad (8)$$

is thus determined. Choosing certain values of the exchange interactions (from the shaded areas in Fig. 3), we show in Fig. 4(a) the calculated $M_{tot}(T)$ for varying in-plane lattice constants imposed by the corresponding substrates. T_{comp} is determined as the temperature at which $M_{tot}(T)$ vanishes. The results are plotted in Fig. 4(b). The shadow illustrates the uncertainties in evaluating the exchange-interaction coefficients. By quantitatively analyzing the contribution from each exchange interaction to T_{comp}, we find that J_{ad} only has marginal influence on the variation of T_{comp} despite its largest magnitude among the exchange parameters. In addition, the influence from J_{aa} and J_{dd} is also negligible. On the contrary, the dominant influence originates from J_{ac} and J_{dc}, whose uncertainties basically determine the shadowed range in Fig. 4(b). This is because T_{comp} arises from the competition of the magnetization of Fe and that of Tb, and the exchange interactions between Fe and Tb (J_{ac} and J_{dc}) determines their relative magnitude of magnetization. The experimentally observed monotonic decrease in T_{comp} with increasing lattice constant a_{sub}, as plotted by the red curve, falls almost completely into the range predicted by the mean-field model with an offset on the absolute values of T_{comp}.

For bulk TbIG, as marked by the pink dashed line, our mean-field simulation yields a range, 256 ∼ 286K, for T_{comp}. Compared to the experimentally measured $T_{comp} = 246$ K [58], this is overestimation which can be understood as following. Due to the lack of magnon-magnon interaction, which lowers the total energy of the system and in turn softens the magnon spectrum with increasing temperature, the magnetization decreases faster than theoretically predicted by mean-field theory.

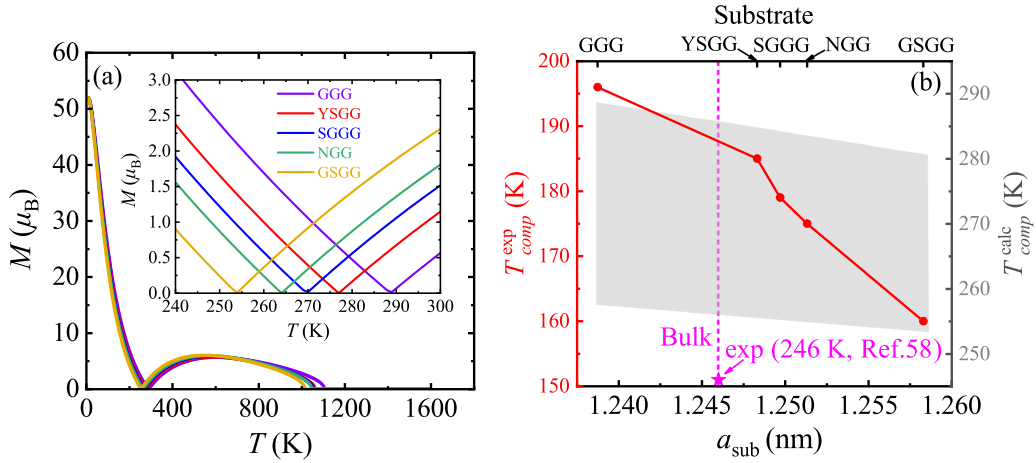

FIG. 4. (a) Calculated total magnetization as function of temperature for distorted TbIG with different in-plane lattice constants as in substrates. Inset enlarges curves around compensation temperature. (b) Measured (left axis) and calculated (right axis) T_{comp} for TbIG as function of (in-plane) substrate lattice constant. Pentagram indicates experimental T_{comp} of bulk TbIG [58].

As the measured T_{comp} on TbIG thin films is much lower than the bulk value [11,32], when comparing the theoretical T_{comp} to the experimental values, we offset the right axis for the calculated values to plot them together with the measured values (left axis) in the same temperature range, i.e., a window of 50 K for both the theoretical results (245 $\sim$ 295 K) and experimental values (150 $\sim$ 200 K) in Fig. 4(b). The measured T_{comp} values of the TbIG films grown on different substrates (red circles) fall into the theoretically calculated range (the shaded area). Satisfactory agreement is found between them, indicating that the main physical mechanism behind the monotonic decrease in the T_{comp} of TbIG with increasing in-plane lattice constant of the substrate is the correspondingly varying exchange interaction. As the substrate changes from GGG to GSGG (lattice size changes from smaller to larger than that of bulk TbIG), the exchange interaction decreases as the bond lengths increase (except for J_{dc}, which is nearly unchanged). In particular, as the lattice constant increases, the exchange field exerted on Tb ions rapidly decreases, leading to a significant decrease in T_{comp}. This may help optimize the spin-orbit torque and facilitate the related applications of ferrimagnetic materials near the compensation temperature [20].

The systematically lower T_{comp} of TbIG thin films, despite various substrates, compared to the bulk value can be attributed to oxygen vacancies [11,32], which are generally present in garnet films [59,60]. We therefore further take into account the oxygen vacancy in our mean-field calculations. Here, we make a simple assumption that the superexchange interaction between the magnetic ions via an oxygen ion vanishes if the oxygen ion is absent. In bulk TbIG, each oxygen ion is shared by one $\mathrm{Fe^O}$, one $\mathrm{Fe^T}$, and two Tb ions. Introducing one such vacancy breaks the exchange between two pairs with J_{ac}, one pair with J_{dc} and one pair with J_{ad}. We thus simulate oxygen vacancy effects by ignoring the field contributed by these exchange interactions. Recalculating T_{comp} for bulk TbIG as a function of the oxygen vacancy amount, as shown in Fig. 5, we find a linear decay in T_{comp}. A few percent of oxygen vacancies leads to a decrease in T_{comp} by tens of degrees Kelvin. One can expect a certain amount of oxygen vacancies in TbIG/Pt films, as it was previously observed that $\mathrm{Fe^0}$, instead of $\mathrm{Fe^{3+}}$ or $\mathrm{Fe^{2+}}$, accumulates at the interface between yttrium iron garnet and Pt films [61]. In addition, Fe depletion from garnet and diffusion into Pt [61] also lowers the field exerted on Tb ions and in turn reduces T_{comp}. The offsets of the vertical axis in Fig. 4(b) are accordingly justified.

VI. CONCLUSIONS

In summary, we manipulate the lattice constant of ferrimagnet garnet TbIG thin films by choosing appropriate garnet substrates, which results in consecutive tuning of the in-plane strain. The XRD, RSM, and STEM measurements confirm the exquisite epitaxial growth of TbIG films and imply a fully strained pseudomorphic structure with in-plane lattice constants equal to those of the substrates. By examining the sign-change temperature of R_{AH} in the TbIG/Pt heterostructure, we accurately determine the compensation temperatures

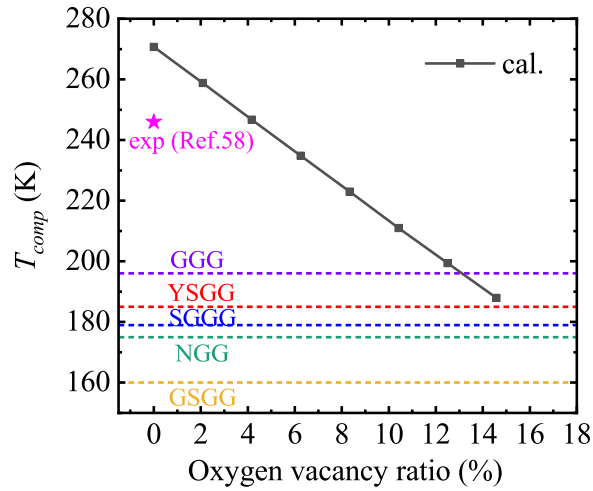

FIG. 5. Calculated compensation temperature of bulk TbIG as function of oxygen vacancy ratio. Dotted lines represent experimental values of TbIG thin films on various substrates. Pentagram denotes measured value for bulk TbIG from Ref. [58].

of TbIG on these substrates with a precision down to 1 K. The compensation temperature monotonically decreases with increasing lattice constant. Density-functional calculations show that the exchange-interaction parameters between different magnetic sublattices exhibit a sensitive dependence on the lattice constant or bond length. This approach not only provides an accurate means of determining the compensation temperature of ReIG films but also enables modulation of the compensation temperature by means of strain. Our findings in this work show the significant potential of ferrimagnetic-insulator based spintronics and practical applications.

ACKNOWLEDGMENTS

Y.L. and Z.S. would like to thank Lili Lang for her assistance on the STEM measurements. Work at Tongji University was supported by the National Key Research and Development Program of China (Grant No. 2022YFA1204002) and National Natural Science Foundation of China, Grants No. 12074285, No. 12374118, and No. 11774259. Work at Beijing Normal University was supported by National Natural Science Foundation of China, Grants No.12174028 and No. 12374101.

[1] A. Manchon, J. Železný, I. M. Miron, T. Jungwirth, J. Sinova, A. Thiaville, K. Garello, and P. Gambardella, Current-induced spin-orbit torques in ferromagnetic and antiferromagnetic systems, Rev. Mod. Phys. **91**, 035004 (2019).

[2] J. Finley and L. Liu, Spintronics with compensated ferrimagnets, Appl. Phys. Lett. **116**, 110501 (2020).

[3] Y. Yang, T. Liu, L. Bi, and L. Deng, Recent advances in development of magnetic garnet thin films for applications in spintronics and photonics, J. Alloys Compd. **860**, 158235 (2021).

[4] Q. Shao, P. Li, L. Liu, H. Yang, S. Fukami, A. Razavi, H. Wu, K. Wang, F. Freimuth, Y. Mokrousov, M. D. Stiles, S. Emori, A. Hoffmann, J. Akerman, K. Roy, J.-P. Wang, S.-H. Yang, K. Garello, and W. Zhang, Roadmap of spin–orbit torques, IEEE Trans. Magn. **57**, 1 (2021).

[5] B. Y. Sokolov and M. Z. Sharipov, Technical magnetization of $Tb_3Fe_5O_{12}$ garnet ferrite near the magnetic compensation point, Tech. Phys. **58**, 1274 (2013).

[6] L. Liensberger, A. Kamra, H. Maier-Flaig, S. Geprags, A. Erb, S. T. B. Goennenwein, R. Gross, W. Belzig, H. Huebl, and M. Weiler, Exchange-enhanced ultrastrong magnon-magnon coupling in a compensated ferrimagnet, Phys. Rev. Lett. **123**, 117204 (2019).

[7] D. Wesenberg, T. Liu, D. Balzar, M. Wu, and B. L. Zink, Long-distance spin transport in a disordered magnetic insulator, Nat. Phys. **13**, 987 (2017).

[8] J. Yu, D. Bang, R. Mishra, R. Ramaswamy, J. H. Oh, H. J. Park, Y. Jeong, P. Van Thach, D. K. Lee, G. Go, S. W. Lee, Y. Wang, S. Shi, X. Qiu, H. Awano, K. J. Lee, and H. Yang, Long spin coherence length and bulk-like spin-orbit torque in ferrimagnetic multilayers, Nat. Mater. **18**, 29 (2019).

[9] C. O. Avci, A. Quindeau, C. F. Pai, M. Mann, L. Caretta, A. S. Tang, M. C. Onbasli, C. A. Ross, and G. S. Beach, Current-induced switching in a magnetic insulator, Nat. Mater. **16**, 309 (2017).

[10] W. Liu, B. Cheng, S. Ren, W. Huang, J. Xie, G. Zhou, H. Qin, and J. Hu, Thermally assisted magnetization control and switching of $Dy_3Fe_5O_{12}$ and $Tb_3Fe_5O_{12}$ ferrimagnetic garnet by low density current, J. Magn. Magn. Mater. **507**, 166804 (2020).

[11] S. Damerio and C. O. Avci, Sputtered terbium iron garnet films with perpendicular magnetic anisotropy for spintronic applications, J. Appl. Phys. **133**, 073902 (2023).

[12] J. S. B. Andlauer and W. Wettling, Optical and magneto-optical properties of YIG and $FeBO_3$, Appl. Phys. **10**, 189 (1976).

[13] B. Y. Sokolov and M. Z. Sharipov, Magneto-optical properties of the iron garnet $Tb_3Fe_5O_{12}$ near the magnetic compensation temperature, Phys. Solid State **56**, 975 (2014).

[14] B. W. Dong, J. Cramer, K. Ganzhorn, H. Y. Yuan, E. J. Guo, S. T. B. Goennenwein, and M. Klaui, Spin Hall magnetoresistance in the non-collinear ferrimagnet GdIG close to the compensation temperature, J. Phys.: Condens. Matter **30**, 035802 (2018).

[15] D. Chen, Y. Xu, S. Tong, W. Zheng, Y. Sun, J. Lu, N. Lei, D. Wei, and J. Zhao, Noncollinear spin state and unusual magnetoresistance in ferrimagnet Co-Gd, Phys. Rev. Mater. **6**, 014402 (2022).

[16] E. R. Rosenberg, L. Beran, C. O. Avci, C. Zeledon, B. Song, C. Gonzalez-Fuentes, J. Mendil, P. Gambardella, M. Veis, C. Garcia, G. S. D. Beach, and C. A. Ross, Magnetism and spin transport in rare-earth-rich epitaxial terbium and europium iron garnet films, Phys. Rev. Mater. **2**, 094405 (2018).

[17] M. V. Logunov, S. S. Safonov, A. S. Fedorov, A. A. Danilova, N. V. Moiseev, A. R. Safin, S. A. Nikitov, and A. Kirilyuk, Domain wall motion across magnetic and spin compensation points in magnetic garnets, Phys. Rev. Appl. **15**, 064024 (2021).

[18] E. A. Mashkovich, K. A. Grishunin, A. K. Zvezdin, T. G. H. Blank, A. G. Zavyalov, P. H. M. van Loosdrecht, A. M. Kalashnikova, and A. V. Kimel, Terahertz-driven magnetization dynamics of bismuth-substituted yttrium iron-gallium garnet thin film near a compensation point, Phys. Rev. B **106**, 184425 (2022).

[19] T. Fu, S. Li, X. Feng, Y. Cui, J. Yao, B. Wang, J. Cao, Z. Shi, D. Xue, and X. Fan, Complex anomalous Hall effect of CoGd alloy near the magnetization compensation temperature, Phys. Rev. B **103**, 064432 (2021).

[20] T. Xu, Y. Cheng, Y. Dong, H. Bai, H.-A. Zhou, X. Shu, P. Gargiani, M. Valvidares, P. Yu, and W. Jiang, Evolution of compensated magnetism and spin-torque switching in ferrimagnetic $Fe_{1-x}Tb_x$, Phys. Rev. Appl. **19**, 034088 (2023).

[21] G. F. Dionne, *Magnetic Oxides* (Springer, New York, 2009), pp. 153–157.

[22] R. Ramos, T. Hioki, Y. Hashimoto, T. Kikkawa, P. Frey, A. J. E. Kreil, V. I. Vasyuchka, A. A. Serga, B. Hillebrands, and E. Saitoh, Room temperature and low-field resonant enhancement of spin Seebeck effect in partially compensated magnets, Nat. Commun. **10**, 5162 (2019).

[23] B. Khurana, J. J. Bauer, P. Zhang, T. Safi, C.-T. Chou, J. T. Hou, T. Fakhrul, Y. Fan, L. Liu, and C. A. Ross, Magnetism and spin

transport in platinum/scandium-substituted terbium iron garnet heterostructures, Phys. Rev. Mater. **5**, 084408 (2021).

[24] J. H. Lee, L. Marcano, R. Aeschlimann, M.-A. Mawass, C. Luo, A. Gloter, J. Varignon, F. Radu, S. Valencia, and M. Bibes, Strain tuning of Néel temperature in $YCrO_3$ epitaxial thin films, APL Mater. **10**, 081101 (2022).

[25] M. Kubota, A. Tsukazaki, F. Kagawa, K. Shibuya, Y. Tokunaga, M. Kawasaki, and Y. Tokura, Stress-induced perpendicular magnetization in epitaxial iron garnet thin films, Appl. Phys. Express **5**, 103002 (2012).

[26] S. Mokarian Zanjani and M. C. Onbaşlı, Predicting new iron garnet thin films with perpendicular magnetic anisotropy, J. Magn. Magn. Mater. **499**, 166108 (2020).

[27] See Supplemental Material at http://link.aps.org/supplemental/10.1103/PhysRevB.108.184403 for the main text, including details of sample preparation, characterization of microstructures, magnetism, and R_H - H loops, and additional theoretical calculations data.

[28] C. Tang, P. Sellappan, Y. Liu, Y. Xu, J. E. Garay, and J. Shi, Anomalous Hall hysteresis in $Tm_3Fe_5O_{12}$/Pt with strain-induced perpendicular magnetic anisotropy, Phys. Rev. B **94**, 140403(R) (2016).

[29] Y. M. Lu, Y. Choi, C. M. Ortega, X. M. Cheng, J. W. Cai, S. Y. Huang, L. Sun, and C. L. Chien, Pt magnetic polarization on $Y_3Fe_5O_{12}$ and magnetotransport characteristics, Phys. Rev. Lett. **110**, 147207 (2013).

[30] A. Quindeau, C. O. Avci, W. Liu, C. Sun, M. Mann, A. S. Tang, M. C. Onbasli, D. Bono, P. M. Voyles, Y. Xu, J. Robinson, G. S. D. Beach, and C. A. Ross, $Tm_3Fe_5O_{12}$/Pt heterostructures with perpendicular magnetic anisotropy for spintronic applications, Adv. Electron. Mater. **3**, 1600376 (2016).

[31] Q. Shao, C. Tang, G. Yu, A. Navabi, H. Wu, C. He, J. Li, P. Upadhyaya, P. Zhang, S. A. Razavi, Q. L. He, Y. Liu, P. Yang, S. K. Kim, C. Zheng, Y. Liu, L. Pan, R. K. Lake, X. Han, Y. Tserkovnyak, J. Shi, and K. L. Wang, Role of dimensional crossover on spin-orbit torque efficiency in magnetic insulator thin films, Nat. Commun. **9**, 3612 (2018).

[32] Y. K. Liu, H. F. Wong, K. K. Lam, K. H. Chan, C. L. Mak, and C. W. Leung, Anomalous Hall effect in Pt/$Tb_3Fe_5O_{12}$ heterostructure: Effect of compensation point, J. Magn. Magn. Mater. **468**, 235 (2018).

[33] H. Chen, D. Cheng, H. Yang, D. Wang, S. Zhou, Z. Shi, and X. Qiu, Magnetization switching induced by magnetic field and electric current in perpendicular TbIG/Pt bilayers, Appl. Phys. Lett. **116**, 112401 (2020).

[34] V. H. Ortiz, M. Aldosary, J. Li, Y. Xu, M. I. Lohmann, P. Sellappan, Y. Kodera, J. E. Garay, and J. Shi, Systematic control of strain-induced perpendicular magnetic anisotropy in epitaxial europium and terbium iron garnet thin films, APL Mater. **6**, 121113 (2018).

[35] X. Zhou, L. Ma, Z. Shi, W. J. Fan, J.-G. Zheng, R. F. L. Evans, and S. M. Zhou, Magnetotransport in metal/insulating-ferromagnet heterostructures: Spin Hall magnetoresistance or magnetic proximity effect, Phys. Rev. B **92**, 060402(R) (2015).

[36] V. H. Ortiz, B. Arkook, J. Li, M. Aldosary, M. Biggerstaff, W. Yuan, C. Warren, Y. Kodera, J. E. Garay, I. Barsukov, and J. Shi, First- and second-order magnetic anisotropy and damping of europium iron garnet under high strain, Phys. Rev. Mater. **5**, 124414 (2021).

[37] H. Wang, C. Du, P. C. Hammel, and F. Yang, Strain-tunable magnetocrystalline anisotropy in epitaxial $Y_3Fe_5O_{12}$ thin films, Phys. Rev. B **89**, 134404 (2014).

[38] Z. Xu, Q. Liu, Y. Ji, X. Li, J. Li, J. Wang, and L. Chen, Strain-tunable interfacial Dzyaloshinskii-Moriya interaction and spin-Hall topological Hall effect in Pt/$Tm_3Fe_5O_{12}$ heterostructures, ACS Appl. Mater. Interfaces **14**, 16791 (2022).

[39] N. M. Vu, P. B. Meisenheimer, and J. T. Heron, Tunable magnetoelastic anisotropy in epitaxial (111) $Tm_3Fe_5O_{12}$ thin films, J. Appl. Phys. **127**, 153905 (2020).

[40] N. W. Ashcroft and N. D. Mermin, *Solid State Physics* (Holt-Saunders International Editions, Philadelphia, 1976).

[41] C. Kittel, *Introduction to Solid State Physics/Charles Kittel*, 8th ed. (John Wiley and Sons Inc., New York, 2005), pp. 336–340.

[42] L.-W. Wang, L.-S. Xie, P.-X. Xu, and K. Xia, First-principles study of magnon-phonon interactions in gadolinium iron garnet, Phys. Rev. B **101**, 165137 (2020).

[43] L.-S. Xie, G.-X. Jin, L. He, G. E. W. Bauer, and K. Xia, First-principles study of exchange interactions of yttrium iron garnet, Phys. Rev. B **95**, 014423 (2017).

[44] A. Cong, J. Liu, W. Xue, H. Liu, Y. Liu, and K. Shen, Exchange-mediated magnon-phonon scattering in monolayer CrI_3, Phys. Rev. B **106**, 214424 (2022).

[45] Y. Liu, L.-S. Xie, Z. Yuan, and K. Xia, Magnon-phonon relaxation in yttrium iron garnet from first principles, Phys. Rev. B **96**, 174416 (2017).

[46] G. Kresse and J. Hafner, *Ab initio* molecular dynamics for liquid metals, Phys. Rev. B: Condens. Matter **47**, 558 (1993).

[47] G. Kresse, Efficient iterative schemes for *ab initio* total-energy calculations using a plane-wave basis set, Phys. Rev. B **54**, 11169 (1996).

[48] K. B. John, P. Perdew, and M. Ernzerhof, Generalized gradient approximation made simple, Phys. Rev. Lett. **77**, 3865 (1996).

[49] P. E. Blöchl, Projector augmented-wave method, Phys. Rev. B **50**, 17953 (1994).

[50] R. Nakamoto, B. Xu, C. Xu, H. Xu, and L. Bellaiche, Properties of rare-earth iron garnets from first principles, Phys. Rev. B **95**, 024434 (2017).

[51] C. M. Srivastava, C. Srinivasan, and R. Aiyar, Exchange constants in ferrimagnetic garnets, J. Appl. Phys. **53**, 781 (1982).

[52] J. B. Goodenough, An interpretation of the magnetic properties of the perovskite-type mixed crystals $La_{1-x}Sr_xCoO_{3-\lambda}$, J. Phys. Chem. Solids **6**, 287 (1958).

[53] J. Kanamori, Superexchange ineraction and symmetry properties of electron orbitals, J. Phys. Chem. Solids **10**, 87 (1959).

[54] J. B. Goodenough, *Magnetism and the Chemical Bond* (John Wiley & Sons, Inc., New York, 1963).

[55] A. B. Harris, Spin-wave spectra of yttrium and gadolinium iron garnet, Phys. Rev. **132**, 2398 (1963).

[56] G. F. Dionne, Molecular field and exchange constants of Gd^{3+}-substituted ferrimagnetic garnets, J. Appl. Phys. **42**, 2142 (1971).

[57] T. Bayaraa, C. Xu, D. Campbell, and L. Bellaiche, Tuning magnetization compensation and Curie temperatures in epitaxial rare earth iron garnet films, Phys. Rev. B **100**, 214412 (2019).

[58] S. Geller, J. P. Remeika, R. C. Sherwood, H. J. Williams, and G. P. Espinosa, Magnetic study of the heavier rare-earth iron garnets, Phys. Rev. **137**, A1034 (1965).

[59] M. Kubota, K. Shibuya, Y. Tokunaga, F. Kagawa, A. Tsukazaki, Y. Tokura, and M. Kawasaki, Systematic control of stress-induced anisotropy in pseudomorphic iron garnet thin films, J. Magn. Magn. Mater. **339**, 63 (2013).

[60] S. Tan, W. Zhang, L. Yang, J. Chen, and Z. Wang, Intrinsic defects in yttrium iron garnet: A first-principles study, J. Appl. Phys. **128**, 183904 (2020).

[61] L. Liu, Y. Li, Y. Liu, T. Feng, J. Xu, X. R. Wang, D. Wu, P. Gao, and J. Li, Interfacial modulation of spin pumping in YIG/Pt, Phys. Rev. B **102**, 014411 (2020).